DOI:10.1190/segam2020-3419985.1

Recovering stratigraphy orientation using TTI 3D CSEM Gauss-Newton inversion

A.K. Bjørke, K.R. Hansen, J.P. Morten, EMGS ASA, Norway

Summary

In areas with high electric anisotropy and/or steep bedding dip angles, there are significant TTI anisotropy effects in marine CSEM data. We show how TTI medium parameterization can be incorporated in 3D Gauss-Newton inversion including the recovery of bedding azimuth and dip angles. The inversion regularization has terms to stabilize the solution of the normal equations, and to include a priori information preferring models with smooth bedding dip variations. We apply the TTI inversion to a field data set from the Gulf of Mexico and show that stratigraphy dip and azimuth in agreement with independent seismic information is recovered without any initial model structure. We also compare to a corresponding VTI inversion and observe that the TTI inversion result is fitting the data better.

Introduction

The electrical anisotropy and structural variation in sedimentary rock stratigraphies can give significant effects in electromagnetic measurements. This has been confirmed both from modeling studies (Davydycheva and Frenkel, 2013) and field-data inversion studies considering marine controlled-source electromagnetic (CSEM) measurements (Hansen et al., 2018). The sensitivity to different resistivity components is due to subsurface electric currents flowing in all directions due to the dipole CSEM source and responses recorded in the 3D survey receiver grid. The anisotropy must therefore be properly represented when imaging and interpreting CSEM data.

In areas with dipping formations, the often-used assumption of vertical transversely isotropic (VTI) anisotropy is no longer valid and one must consider the effect of tilted transverse isotropy (TTI). Hansen et al. (2016) showed that TTI anisotropy can be included in a CSEM inversion scheme, and that this is necessary to properly interpret the data. In that work, the implementation utilized a gradient-based optimization which generally necessitates an initial model where the structure is well approximated in areas with strong TTI effects. The information about the structure can be derived from depth migrated seismic data, but such data might not always be readily available. An inversion scheme less dependent on the initial model would therefore be beneficial in this case.

In this paper we show results from a Gauss-Newton inversion scheme (Nguyen et al., 2016) accounting for TTI anisotropy. As we will show, this scheme is able to recover the dip structure without any prior information in the initial model. This reduces the dependence on seismic horizons in an area to do TTI inversion. It will also simplify and speed up the work related to preparing the initial models. Furthermore, since CSEM can be used to determine bedding dip it can act as an independent way to determine stratigraphy structure, complementing seismic.

Geologic settings that require TTI medium description

A range of geologic environments and conditions can generate an electrically anisotropic medium where the conductivity will depend on the direction of the current flow. For hydrocarbon exploration, the clastic environments are of special interest. Deposition processes can lead to grains being oriented along defined directions, and the effect of gravity leads to layering. The electrical anisotropy may subsequently be reinforced by compaction and diagenesis after burial. The importance of accommodating electrical anisotropy to avoid artefacts in inversion (Jing et al., 2008) has already been recognized and has motivated the implementation of inversion codes supporting VTI medium description (Meju et al., 2018).

While the VTI medium description may be adequate in environments where either or both the bedding dip and anisotropy are low, experience from interpreting field data show that the more complex TTI medium description is necessary in many settings. In the Barents Sea, Norway, the electrical anisotropy can be very large, with the ratio of bed-normal relative to bed-parallel resistivity often above 10. With such high anisotropy, even small dip angles of e.g. 5° may generate a measurable TTI effect. Conversely, in regions with large bedding dip, for example fold and thrust belts in the Gulf of Mexico or close to allochthonous salt, significant TTI effects can be generated with even a modest electrical anisotropy ratio e.g. 3, which is commonly encountered in shales.

3D CSEM inversion with TTI media

We have developed a 3D CSEM inversion that incorporates TTI medium parameterization and forward modeling. The parameter fitting for the conductivity and bedding angle is done using a Gauss-Newton optimization scheme, which uses distributed memory systems to make it suitable for the large-scale problems of marine 3D CSEM.

Forward modelling

The forward modelling problem is to solve the Maxwell's equations in the quasi-static limit,

$$\nabla \times \mathbf{E} = -\mu_0 \frac{\partial \mathbf{H}}{\partial t}, \qquad (1)$$

10.1190/segam2020-3419985.1

$$\nabla \times \mathbf{H} = \boldsymbol{\Sigma}\mathbf{E} + \mathbf{J}, \tag{2}$$

where **E** and **H** are the electric and magnetic fields, **J** is the source current density, and $\boldsymbol{\Sigma}$ is the conductivity tensor of the medium. For a TTI medium, the conductivity tensor is diagonal in a coordinate system aligned with the beds, called the principal coordinates (Figure 1), and can be written as

$$\boldsymbol{\Sigma} = \boldsymbol{R}^{\mathrm{T}} \begin{pmatrix} \sigma_p & & \\ & \sigma_p & \\ & & \sigma_n \end{pmatrix} \boldsymbol{R} \tag{3}$$

where $\sigma_p(\mathbf{r})$ and $\sigma_n(\mathbf{r})$ are the bed-parallel and normal components of the conductivity and $\boldsymbol{R}$ is a rotation matrix,

$$\boldsymbol{R}(\alpha,\beta) = \begin{pmatrix} \cos\alpha\cos\beta & \sin\alpha\cos\beta & -\sin\beta \\ -\sin\alpha & \cos\alpha & 0 \\ \cos\alpha\sin\beta & \sin\alpha\sin\beta & \cos\beta \end{pmatrix}. \tag{4}$$

In this matrix, $\alpha(\mathbf{r})$ and $\beta(\mathbf{r})$ are the spatially varying Euler angles that describe the local bedding azimuth and dip.

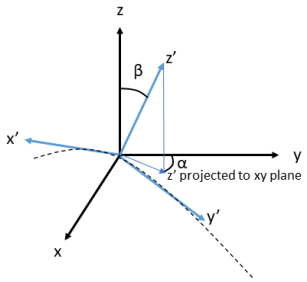

Figure 1 Black lines: Model coordinate system (x, y, z). *Blue lines: Rotated, local coordinate system* (x', y', z') *oriented by the Euler angles* α *and* β. *Dashed line: Bed structure aligned to principal coordinates* (x', y', z').

We solve the forward problem using a finite-difference time domain (FDTD) scheme applied to equations (1) and (2). To speed up the calculation, these equations are transformed from the real-world domain, in which displacement currents are negligible, to a fictitious domain in which conduction currents are negligible (Maaø, 2007). The equations are discretized and solved on a Lebedev grid to accommodate the structure of $\boldsymbol{\Sigma}$, similar to Davydycheva et al. (2003).

Inverse problem

The CSEM inverse problem is formulated as a least-squares optimization with the objective function,

$$\varepsilon(\mathbf{m}) = \varepsilon_d(\mathbf{m}) + \lambda^{\sigma}\varepsilon_r^{\sigma}(\mathbf{m}) + \lambda^{(\alpha,\beta)}\varepsilon_r^{(\alpha,\beta)}(\mathbf{m}), \tag{5}$$

where $\mathbf{m} = \boldsymbol{f}\left(\left[\boldsymbol{\sigma}_n{}^{\mathrm{T}}, \boldsymbol{\sigma}_p{}^{\mathrm{T}}, \boldsymbol{\alpha}^{\mathrm{T}}, \boldsymbol{\beta}^{\mathrm{T}}\right]^{\mathrm{T}}\right)$ is the vector of parameters to be fitted by the inversion on the discretized grid, and the subscripts *d* and *r* denote data and regularization terms. The non-linear function $\boldsymbol{f}$ ensures that parameters are within bounds for conductivity (Abubakar et al., 2009) and wrapped correctly for angles. The regularization contribution is split in a part ε_r^{σ} for the conductivity values and a part $\varepsilon_r^{(\alpha,\beta)}$ for the Euler angles. The pre-factors λ^{σ} and $\lambda^{(\alpha,\beta)}$ are scaling parameters for the regularization strength.

The data term in the objective function is,

$$\varepsilon_d(\mathbf{m}) = \frac{1}{N_d}(\Delta\mathbf{d})^{\dagger}\boldsymbol{W}_d^{T}\boldsymbol{W}_{\boldsymbol{d}}(\Delta\mathbf{d}) \tag{6}$$

where $\Delta\mathbf{d} = \mathbf{d}^{\mathrm{obs}} - \mathbf{d}^{\mathrm{syn}}(\mathbf{m})$ is a vector of the difference between the synthetic data for the given model **m** and the observed data. N_d is the number of data points and $\mathbf{W}_{\mathrm{d}}$ is a diagonal weighting matrix with the inverse of the data standard deviations along the diagonal (Hansen et al., 2018). The ε_r^{σ} term discretizes an approximate *L*-norm of gradients,

$$\varepsilon_r^{\sigma}(\mathbf{m}^{\sigma}) \approx \frac{1}{V}\int \|\boldsymbol{A}\nabla'(\mathbf{m}^{\sigma} - \mathbf{m}_{\mathrm{AP}}^{\sigma})\|_L dV\,, \tag{7}$$

where $V = \sum_i V_i$ is the volume of the model summed over the parameter cell indices i, $\mathbf{m}^{\sigma}$ is the conductivity part of the parameter vector, the matrix $\boldsymbol{A}$ contains directional weights for the gradient operator $\nabla' = \boldsymbol{R}\nabla$ with respect to the local bedding-aligned coordinate system (Causse et al., 2019), and $\mathbf{m}_{\mathrm{AP}}^{\sigma}$ is an *a priori* model typically coinciding with the initial model for the inversion. By evaluating this regularization contribution in terms of the local bedding-aligned gradient of the conductivity rather than the gradient in the model coordinate system, we ensure layer continuity and smoothness along the formation dip which is important for proper imaging of steeply dipping structure.

Angle regularization

In the TTI inversion, we introduce two additional angle optimization parameters $\alpha(\mathbf{r})$ and $\beta(\mathbf{r})$. The angle regularization $\varepsilon_r^{(\alpha,\beta)}(\mathbf{m})$ is composed of two contributions. The first term penalizes deviation from an *a priori* structure. This regularization contribution will stabilize the inversion by making the Hessian for the Gauss-Newton optimization non-singular and is,

$$\varepsilon_{r1}^{(\alpha,\beta)} = \frac{1}{V}\Sigma_i \left|\left|W_i^R\left[\boldsymbol{R}_i(\alpha_i,\beta_i) - \boldsymbol{R}_i(\alpha_i^{\mathrm{AP}},\beta_i^{\mathrm{AP}})\right]\right|\right|^2 V_i. \tag{8}$$

Here W_i^R is an appropriate weight for the cell with index i. The implementation in terms of the $\boldsymbol{R}$ matrix elements

DOI:10.1190/segam2020-3419985.1

eliminates a model null-space due to $n\pi$ ambiguities of the angles. As for the conductivity values, the α_i^{AP} and β_i^{AP} *a priori* angle distributions typically correspond to the initial model bedding dip.

A second angle regularization term called the minimum angle gradient is included to prefer models with smooth bedding dip variations and as few abrupt angle changes as required by the data. This is achieved by minimizing the L2 norm of the spatial derivatives of the bedding-normal vector,

$$\mathbf{n}(\alpha,\beta) = \begin{bmatrix} \cos\alpha \sin\beta \\ \sin\alpha \sin\beta \\ \cos\beta \end{bmatrix}. \tag{9}$$

The regularization contribution is calculated as

$$\varepsilon_{r2}^{(\alpha,\beta)} = \frac{1}{V}\Sigma_i \left(\left|\left|W_i^{nx}\partial_x \mathbf{n}_i\right|\right|^2 + \left|\left|W_i^{ny}\partial_y \mathbf{n}_i\right|\right|^2 + \left|\left|W_i^{nz}\partial_z \mathbf{n}_i\right|\right|^2 \right) V_i, \tag{10}$$

where the $W_i^{n(x,y,z)}$ pre-factors give an appropriate weight to each parameter cell and can also control different penalization to angle variation in the different directions. We have found that this regularization term gives good flexibility to limit undesired variation while also offering convenient computational properties.

Inversion update algorithm

The objective function minimization is achieved using a Gauss-Newton algorithm (Nguyen et.al. 2016). A TTI inversion approach utilizing the L-BFGS-B algorithm (Zhu et al., 1997) to estimate parameter update based on gradients was described by Hansen et al. (2018, 2016). The Jacobian elements for the bedding-aligned conductivities and the Euler angles are determined in terms of the $\boldsymbol{\Sigma}$ elements by applying the chain rule and the matrix $\boldsymbol{R}$. The Gauss-Newton approach used by the inversion described here achieves a better Hessian matrix estimation. One advantage of this higher order model update algorithm is the ability to effectively compute parameter updates in model domains with low sensitivity. Further, this algorithm is more robust with respect to the choice of the initial model. Therefore, the inversion algorithm described in this paper can be deployed to recover structure in complicated environments and does not require seismic information to constrain the initial model bedding dip. As we will demonstrate, the recovered structure models may even be used as independent structure information to interpret in conjunction with seismic.

Field data inversion example

We apply the described inversion scheme to a field data set from the Gulf of Mexico. The survey data used in the inversion includes horizontal electric field measurements from 184 receivers spaced 1.5 km apart, and 24 source towlines. We included the frequencies 0.156 Hz, 0.469 Hz and 0.781 Hz. Data points with source-receiver offset up to 13 km were included in the optimization.

We have carried out both VTI and TTI inversion so that we can compare the results in terms of geological feasibility and data fit. In the VTI inversion, the dip angles are constant at 0° in agreement with the medium representation. The resistivity components from VTI inversion is shown in Figure 2. The result of the TTI inversion, where also the α, β angles are recovered, is shown in Figure 3. Both inversions were started from an initial half-space model with vertical/normal resistivity 1.25 Ωm and horizontal/parallel resistivity 1.0 Ωm. For the TTI inversion the initial values for the α and β values were both 0°.

There are noticeable differences between both the values and structure of the subsurface resistivity models resulting from the VTI and the TTI inversions. The TTI inversion recovers a shallow layer with normal resistivity about 1-1.2 Ωm, and an increased resistivity $\approx$ 5 Ωm starting around 1500 m below the mudline. This transition follows the seismic mapped stratigraphy closely, which reinforces the plausibility of such structure. The VTI inversion shows several high resistive, localized anomalies at the slopes of the seismic mapped structures, with resistivities up to 30 Ωm. Such a systematic pattern of localized resistivity anomalies correlating with structure in both the normal and the horizontal resistivity does not seem very reasonable, and we interpret that these as imaging artefacts resulting from the invalid VTI medium assumption. These artefacts could have been misinterpreted as hydrocarbon-charged traps but are not present in the TTI result which achieves a better data fit.

A different section from the same data set was shown by Hansen et al. (2018), where the gradient-based optimization scheme was utilized. In that application, it was necessary to provide the inversion with a realistic initial model to achieve a good data fit. The initial model resistivity variation incorporated a linear depth increase following the main features of the seismic mapped stratigraphy, and the angle values for the TTI dip and azimuth model were estimated from interpreted seismic depth horizons for the area. The dip angles in the initial model were up to 50°, and only minor changes to these angles were obtained in the inversion.

Using our current TTI Gauss-Newton inversion scheme, we achieve similar results when starting from a simple half-space model with no structure (dip angle 0°), which significantly simplifies the processes of setting up the inversion. The good agreement between the inversion result and the seismic interpreted structure (Figure 3) also demonstrates how the CSEM data can independently determine structure to corroborate seismic interpretation.

10.1190/segam2020-3419985.1

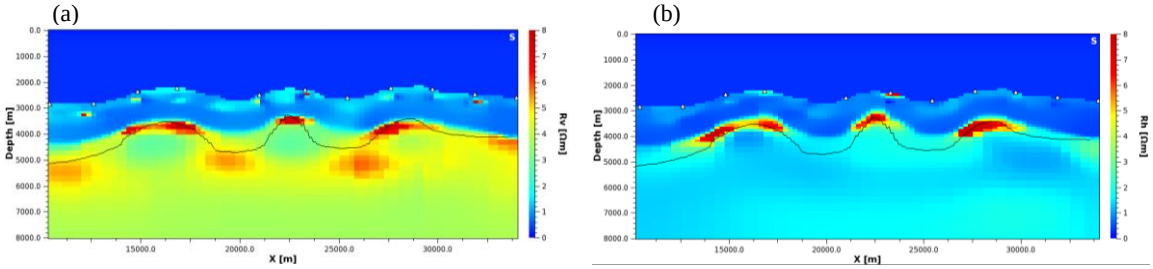

Figure 2: 2D section through the resulting vertical (a) and horizontal 3D resistivity model (b) for the VTI reference inversion. The overall data fit obtained for this inversion was 1.75, obtained after 23 Gauss-Newton iterations. The small white triangles indicate the position of receivers. The black line is a horizon obtained from seismic, which was not used in the inversion.

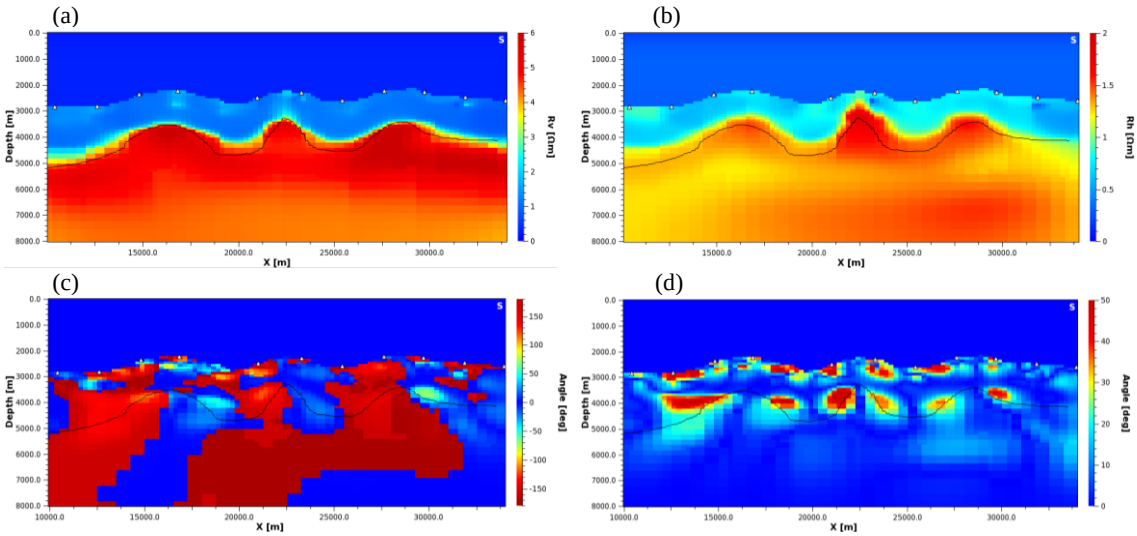

Figure 3: 2D section through the resulting normal (a) and parallel 3D resistivity model (b), azimuth angle α (c) and dip angle β (d) from the TTI inversion. The data fit for this model is 1.35, so this model is describing the data better than the model obtained from the VTI inversion, and convergence was achieved after 22 Gauss-Newton iteration steps. The β angles are close to the original value of 0 in the deep part of the model due to limited sensitivity, and consequently there are no sensitivity to the α angles. In the shallow, less resistive zone, the anisotropy factor is low (varying from 1.0 to 1.4), which gives less sensitivity to the orientation angles. This explains the limited update in beta angles for this depth range.

Conclusions

We have implemented a 3D Gauss-Newton inversion scheme, which takes TTI anisotropy fully into account. To stabilize the solution of the normal equations and avoid artefacts in the recovered angle parameters, regularization of the dip and azimuth angles is applied.

Unlike previously published gradient-based inversion schemes with TTI medium description, the inversion can update the bedding azimuth and dip angle from an initial model containing no information on the structure. This enables the use of the inversion in areas with little or no reliable structural a priori information.

The described inversion scheme has been applied to a field data set from the Gulf of Mexico. The inversion model results show plausible structural updates for the TTI inversion but unrealistic localized anomalies for the VTI inversion. The TTI inversion also obtains a much better data fit than the corresponding VTI inversion.

Acknowledgments

We thank EMGS for permission to publish this paper. We also thank our colleagues Martin Panzner and Jürg Hunziker for helpful discussions about TTI inversion.

REFERENCES

Abubakar, A., T. M. Habashy, M. Li, and J. Liu, 2009, Inversion algorithms for large-scale geophysical electromagnetic measurements: Inverse Problems, **25**, 123012.

Causse, E., J. I. Nordskag, and K. R. Hansen, 2019, 3D Gauss-Newton inversion of CSEM data with structural regularization: 81st Conference and Exhibition, EAGE, Extended Abstracts, 1–5.

Davydycheva, S., V. Druskin, and T. M. Habashy, 2003, An efficient finite-difference scheme for electromagnetic logging in 3D anisotropic inhomogeneous media: Geophysics, **68**, 1525–1536.

Davydycheva, S., and M. A. Frenkel, 2013, The impact of 3D tilted resistivity anisotropy on marine CSEM measurements: The Leading Edge, **32**, 1374.

Hansen, K., M. Panzner, D. Shantsev, and R. Mittet, 2016, TTI inversion of marine CSEM data: 86th Annual International Meeting, SEG, Expanded Abstracts, 1014–1018, doi: https://doi.org/10.1190/segam2016-13858558.1.

Hansen, K. R., M. Panzner, D. Shantsev, and K. Mohn, 2018, Comparison of TTI and VTI 3D inversion of CSEM data: 80th Conference and Exhibition, EAGE, Extended Abstracts, 1–5.

Jing, C., K. Green, and D. Willen, 2008, CSEM inversion: Impact of anisotropy, data coverage, and initial models: 78th Annual International Meeting, SEG, Expanded Abstracts, 604–608, doi: https://doi.org/10.1190/1.3063724.

Maaø, F. A, 2007, Fast finite-difference time-domain modeling for marine-subsurface electromagnetic problems: Geophysics, **72**, no. 2, A19–A23.

Meju, M. A., R. V. Miller, S. Shukri, N. K. S. Mansor, J. H. W. Kho, and S. Shahar, 2018, Unconstrained 3D anisotropic CSEM resistivity inversion: Industry benchmark: 80th Conference and Exhibition, EAGE, Extended Abstracts, 1–5.

Nguyen, A. K., J. Iren Nordskag, T. Wiik, A. K. Bjørke, L. Boman, O. M. Pedersen, J. Ribaudo, and R. Mittet, 2016, Comparing large-scale 3D Gauss–Newton and BFGS CSEM inversions: 86th Annual International Meeting, SEG, Expanded Abstracts, 872–877, doi: https://doi.org/10.1190/segam2016-13858633.1.

Zhu, C., R. H. Byrd, P. Lu, and J. Nocedal, 1997, Algorithm 778: L-BFGS-B: Fortran subroutines for large-scale bound-constrained optimization: ACM Transactions on Mathematical Software, **23**, 550–560, doi: https://doi.org/10.1145/279232.279236.